Journal of Colloid and Interface Science 453 (2015) 177–185

Contents lists available at ScienceDirect

Journal of Colloid and Interface Science

www.elsevier.com/locate/jcis

Impact of air and water vapor environments on the hydrophobicity of surfaces

Patricia B. Weisensee [a], Nitin K. Neelakantan [b], Kenneth S. Suslick [b], Anthony M. Jacobi [a], William P. King [a,*]

[a] Department of Mechanical Science and Engineering, University of Illinois at Urbana-Champaign, 1206 W. Green St., Urbana, IL 61801, USA
[b] Department of Chemistry, University of Illinois at Urbana-Champaign, 600 S. Mathews Av., Urbana, IL 61801, USA

GRAPHICAL ABSTRACT

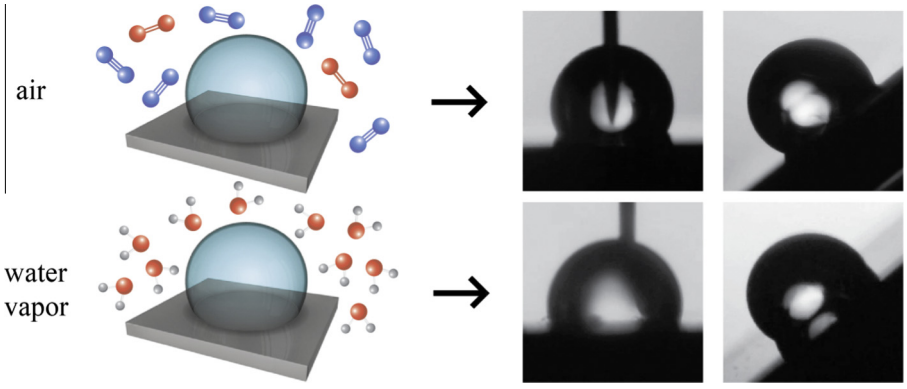

ARTICLE INFO

Article history:
Received 30 March 2015
Accepted 27 April 2015
Available online 4 May 2015

Keywords:
Dynamic contact angle
Superhydrophobic
Wetting
Droplet mobility
Nanoparticle spray
Zinc Oxide (ZnO)
Sliding angle
Vapor adsorption
Teflon
Spreading pressure

ABSTRACT

Hypothesis: Droplet wettability and mobility play an important role in dropwise condensation heat transfer. Heat exchangers and heat pipes operate at liquid–vapor saturation. We hypothesize that the wetting behavior of liquid water on microstructures surrounded by pure water vapor differs from that for water droplets in air.

Experiments: The static and dynamic contact angles and contact angle hysteresis of water droplets were measured in air and pure water vapor environments inside a pressure vessel. Pressures ranged from 60 to 1000 mbar, with corresponding saturation temperatures between 36 and 100 °C. The wetting behavior was studied on four hydrophobic surfaces: flat Teflon-coated, micropillars, micro-scale meshes, and nanoparticle-coated with hierarchical micro- and nanoscale roughness.

Findings: Static advancing contact angles are 9° lower in the water vapor environment than in air on a flat surface. One explanation for this reduction in contact angles is water vapor adsorption to the Teflon. On microstructured surfaces, the vapor environment has little effect on the static contact angles. In all cases, variations in pressure and temperature do not influence the wettability and mobility of the water droplets. In most cases, advancing contact angles increase and contact angle hysteresis decreases when the droplets are sliding or rolling down an inclined surface.

* Corresponding author at: Mechanical Engineering Laboratory, 105 South Mathews Av., Urbana, IL 61801, USA.
E-mail addresses: weisens2@illinois.edu (P.B. Weisensee), neelaka2@illinois.edu (N.K. Neelakantan), ksuslick@illinois.edu (K.S. Suslick), a-jacobi@illinois.edu (A.M. Jacobi), wpk@illinois.edu (W.P. King).

http://dx.doi.org/10.1016/j.jcis.2015.04.060
0021-9797/

Nomenclature

Abbreviations

ZnO	Zinc Oxide
PDMS	polydimethylsiloxane
SEM	scanning electron microscopy
CA	contact angle
CAH	contact angle hysteresis
PTFE	polytetrafluoroethylene

Symbols

γ	surface tension (mN/m)
Θ	contact angle (°)
$\Delta\Theta$	contact angle hysteresis (°)
f	solid–liquid fraction
r	surface roughness ratio
p	pressure (mbar)
T	temperature (°C)
α	tilt angle (°)
$\bar{u}$	average droplet velocity (mm/s)
π	spreading pressure (mN/m)
a	radius of contact area between droplet and solid (mm)
V	droplet volume (μl)
ρ	density (kg/m^3)
g	gravitational constant (m/s^2)

Sub- and superscripts

A	advancing
R	receding
sl	solid–liquid
sg	solid–gas
lg	liquid–gas
s	solid
l	liquid
Y	Young
W	Wenzel
C–B	Cassie–Baxter
d	dispersive

1. Introduction

Dropwise condensation heat transfer has gained renewed attention over the last decade, in particular due to advances in microfabrication and materials synthesis techniques that can produce surfaces that promote droplet formation [1–7]. Compared to filmwise condensation, heat transfer rates during dropwise condensation can be larger by almost an order of magnitude [8,9]. The wettability of the surface and the mobility of the droplets after condensation greatly influence the condensation process. Mobile droplets with high contact angles clean nucleation sites rapidly and thereby allow for high nucleation rates and thus high heat transfer across the surface. Most studies on wettability and mobility of water droplets on micro- and nanostructured surfaces have been performed in air with atmospheric relative humidity [10–18]. Heat exchangers, heat pipes and other systems with two-phase flow, however, operate in a pure vapor environment at saturated conditions. It is thus important to have an understanding of how the gas environment influences the droplet wettability and mobility.

When a small amount of liquid resides on a solid surface, the liquid either spreads or forms discrete droplets. This behavior is governed by the surface tensions γ of the liquid–gas, solid–gas, and solid–liquid interfaces near the three-phase contact line. The equilibrium contact angle (CA) on a flat surface is referred to here as Young's CA Θ_Y and can be thought of as a force balance between the solid–gas γ_{sg}, solid–liquid γ_{sl} and liquid–gas γ_{lg} surface tensions [19]:

$$\cos(\theta_Y) = \frac{\gamma_{sg} - \gamma_{sl}}{\gamma_{lg}} \tag{1}$$

Surfaces on which water will form droplets with $\Theta_Y > 90°$ are considered hydrophobic.

On a real surface, the largest and smallest possible angle for a stationary contact line are the advancing, Θ_A, and receding, Θ_R, contact angle, respectively. The difference between these angles, the contact angle hysteresis (CAH) $\Delta\Theta$, results from energetic barriers to the displacement of the three-phase contact line on non-ideal surfaces [20,21]. Droplets must overcome an activation energy before the contact line moves, which is also known as contact line pinning [22]. The existence of metastable states leads to sessile CAs Θ different from the global equilibrium Θ_Y [22,23]. For deposited droplets, Θ is usually much closer to Θ_A than to Θ_R [24]. On microstructured surfaces, the energy required for advancing is minimal, as the droplets can simply descend (or fall) onto the next post, whereas a receding liquid has to actively unpin or disjoin from the surface before moving. For a given surface, the measured sessile-drop CA can vary between measurements on the same surface by up to 20° due to a range of metastable states, while the measured advancing and receding CAs are typically highly repeatable [22].

Surface roughness and microstructures enhance hydrophobicity. Wenzel showed that with a roughness factor r the apparent contact angle Θ_W, i.e. the angle given for a macroscopic droplet, becomes [25]:

$$\cos(\theta_W) = r\cos(\theta) \tag{2}$$

For textured surfaces with air trapped beneath the droplet and the fractional area of the solid–liquid interface f, the Cassie–Baxter CA Θ_{C-B} is [26]:

$$\cos(\theta_{C-B}) = f\cos(\theta) + f - 1 \tag{3}$$

Liquids can transition between the Cassie–Baxter to the Wenzel state if enough activation energy is provided, for example by drops falling from some height or vibration [27]. Fig. 1 shows water droplets in the Cassie–Baxter state on microstructured surfaces.

This work presents the influence of the gas environment on the static and dynamic wetting behavior of water droplets on four different surface morphologies. The effect of pressure and corresponding saturation temperatures are also analyzed.

2. Materials and methods

2.1. Sample fabrication and characterization

Fig. 2 shows scanning electron microscope (SEM) images of the four micro- and nanostructured samples, i.e., microfabricated silicon micropillars, nanoparticles on a flat surface, and a copper mesh with and without a nanoparticle coating. A flat, Teflon-coated Silicon wafer served as a reference sample. Silicon pillars were fabricated using a Bosch etching process. The square pillars have an edge length of 10 μm, a pitch size of 20 μm and a height of

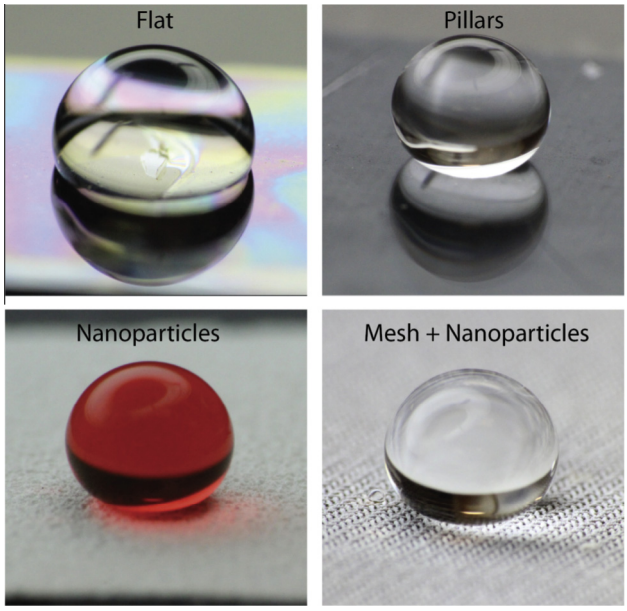

Fig. 1. Images of water droplets (volume 5–10 μl) on four different Teflon coated samples: flat Silicon wafer, silicon pillars, ZnO nanoparticles on a flat Silicon wafer, and ZnO nanoparticles on a 200 mesh. The water droplet on the nanoparticle sample is dyed red for better visualization. (For interpretation of the references to color in this figure legend, the reader is referred to the web version of this article.)

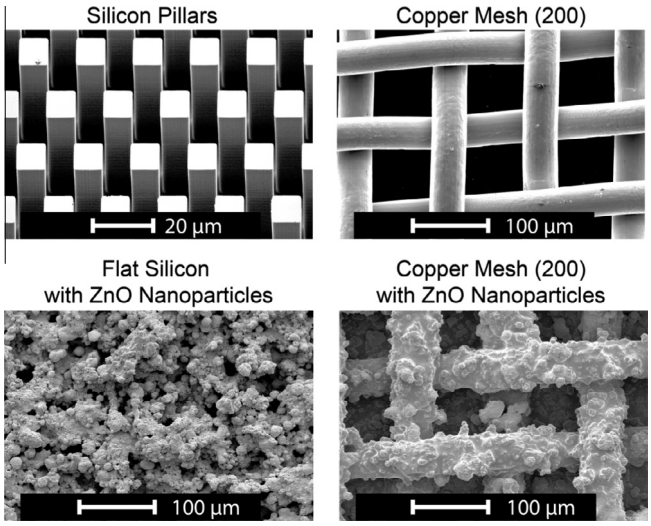

Fig. 2. Scanning electron microscope (SEM) images of the basic samples: $10 \times 20\ \mu m^2$ (pillar size × pitch) square silicon pillars with a height of 30 μm, a 200 mesh with a fiber diameter of 46 μm, a flat silicon wafer coated with a 1:1 ZnO:PDMS nanoparticle spray, and a 200 mesh coated with nanoparticles.

approximately 30 μm. The solid–liquid fraction in the Cassie–Baxter state is $f = 0.25$. Nanoparticle samples consist of Zinc Oxide (ZnO) nanoparticles with an equivalent diameter of 40–100 nm in a polydimethylsiloxane (Sylgard 182) (PDMS) matrix. For the preparation, ZnO and PDMS were mixed together with hexane in a 1:1 w/w solution. The solution was then sprayed onto a flat Silicon wafer and a 200 mesh (TWP Inc.) to create hierarchical micro- and nanostructures. All samples, except for a bare, as-received copper mesh, were dip coated in liquid Teflon from DuPont in a 5:1 solution of FC-770:Teflon AF with 6% solids. The thickness of the Teflon coating on the flat surface is in the order of 100 nm, as determined by profilometry.

Fig. 3 shows the experimental setup in which we measured water droplet contact angles in gas environments of either air or pure water vapor. A light source illuminated the sample on the center stage through one of the windows. A Canon T3i camera with a Sigma 70–300 mm lens and a Raynox DCR-150 macro lens monitored the droplets through a second window at 180° from the first. The frame rate of the recorded images was 60 fps at a pixel resolution of 1280 × 720. The CAs were analyzed using the software DropSnake, which uses active contour B-spline snakes to match the shape of the drop [28]. A 0.2 mL micro-syringe (Gilmont EW-07840-00) with a gauge 33 needle (Hamilton, Metal Hub NDL) positioned the droplets on the surface. A pressure transducer (Omega PX319-100AI; accuracy: ±0.25%) monitored the pressure in the chamber.

The simultaneous control of pressure and temperature in the vacuum chamber allowed for measurements at saturated conditions. The pressure in the chamber, ranging from 60 to 1000 mbar, was controlled manually with a needle valve and a vacuum pump. For the measurements in pure water vapor, a custom built electrical heater (OEM Heaters) maintained water in the bottom of the chamber at the respective saturation temperature. A BriskHeat X2 PID Temperature controller, using a J-type thermocouple as input, controlled the temperature of the liquid over the range of 36–100 °C (±1 °C). A second, T-type thermocouple (Omega TNQSS-125U-6; accuracy: ±0.5 °C) recorded the temperature in the chamber. During the experiments, the vacuum pump was operated continuously to counterbalance evaporation. The fraction of water vapor in the chamber, i.e., the temperature-dependent partial pressure of water vapor divided by the measured pressure in the vacuum chamber, was usually above 92%, and always greater than 76%. For measurements in the air environment, the bottom of the vacuum chamber was left empty and the measurements took place at ambient temperatures and moisture, i.e. relative humidity, conditions within the same pressure range.

Static contact angles were measured by depositing a water droplet of volume $V \approx 5$ μl on the horizontal sample. For the advancing CA, the water volume was slowly increased and for the receding CA the drop volume was slowly reduced while the droplet position remained static. The CAs were measured in the frame before the contact line translated to a new position. All of the reported values

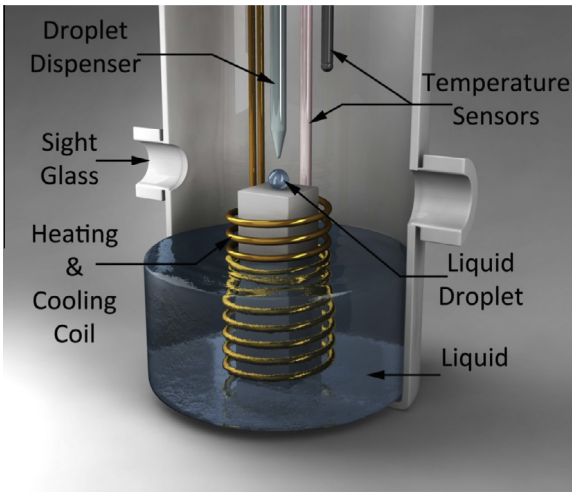

Fig. 3. Vacuum chamber for the experiments in water vapor environment. Liquid water at the bottom of the chamber gets heated by an electrical heater to its saturation temperature while vacuum is pumped continuously at the top of the chamber (not shown). Two thermocouples monitor the temperature in the chamber. A liquid water droplet gets deposited on the sample by a micro-syringe and is captured by a camera through a side glass. The sample is illuminated from the back through a second window.

are averaged over at least four measurements at each pressure level. Their 95% confidence interval, following a *t*-distribution, is given as a measure of uncertainty.

Dynamic CAs were measured for a droplet sliding or rolling down an inclined sample. The angle of inclination of the sample to the horizontal, the tilt angle α, was 1–2° above the respective critical sliding angle for onset of droplet movement. The needle was placed above the sample such that the droplets of volume $V \approx 5$ µl would gently deposit onto the sample. For the samples with nanoparticles, the droplets were placed onto the horizontal surface. Then the setup was slowly rotated until the droplets started rolling off and the tilt angle was recorded. CAs were measured when the droplets reached a quasi-steady-state velocity. Previous reports point out that velocities for small droplets moving along flat or microgrooved surfaces are approximately constant [29,30]. All of the reported CA values are averaged over at least six measurements at each pressure level to account for inhomogeneities in surface structure and variations in droplet velocity.

3. Results and discussion

3.1. Static contact angles

Figs. 4 and 5 show the advancing static CAs and CAH, respectively, on all samples in the air (black) and water vapor (gray) environments. The measured CAs are nearly constant over the studied temperature and pressure range. Table 1 lists the measured static advancing CAs and CAH for all samples in air and in water vapor, averaged over all pressure and temperature conditions. In air, the flat surface has advancing and receding CAs of $\Theta_A/\Theta_R = 116°/103°$, which agree well with values reported elsewhere [31]. The hysteresis on a flat surface in air is thus $\Delta\Theta = 13°$. Both the bare and Teflon-coated meshes have the lowest CAs of all microstructured surfaces. Samples with pillars and nanoparticles achieve CAs between 154° and 159°. As expected, the hysteresis on the pillar sample is relatively large with $\Delta\Theta = 25°$ in air and the droplets are not very mobile [10,22]. Interestingly, the mesh + nanoparticle sample with $\Delta\Theta = 14°$ in air has a higher CAH than the nanoparticle-only sample with $\Delta\Theta = 10°$. Often, dual length scales, i.e. features on both the micro- and nanometer scales, decrease CAH and increase mobility [11,15,32–34]. In the present case, both samples with nanoparticles have features with multiple length scales due to particle agglomeration. The particle density on the mesh, however, is significantly lower than that on the nanoparticle-only sample and the predominant length scale is that of the mesh. The values of the advancing CAs and CAH on the mesh + nanoparticles sample lie thus between those of a mesh without nanoparticles and those of nanoparticles on a flat surface.

In the water vapor environment the advancing CAs on the flat surface are 9° smaller than those in air. We propose that water vapor adsorption to the Teflon causes the apparent surface energy of the solid to rise. When the three-phase contact line moves over the solid with the higher net surface energy, the advancing CA decreases, as can be concluded from Eq. (1). On the microstructured surfaces the gas environment has little to no influence on the wettability of the surface. The advancing CAs in the water vapor environment are at most 2° lower than those in air. Most probably, the active unpinning of the droplets and traversing of a gap during advancing reduces the effect of higher surface energy ahead of the droplet. Also, the contact area between liquid and Teflon is significantly lower than on a flat surface, reducing the influence of the solid's surface energy on the CA. After removal from the vapor environment and subsequent drying, the CAs of all samples returned to their values in air.

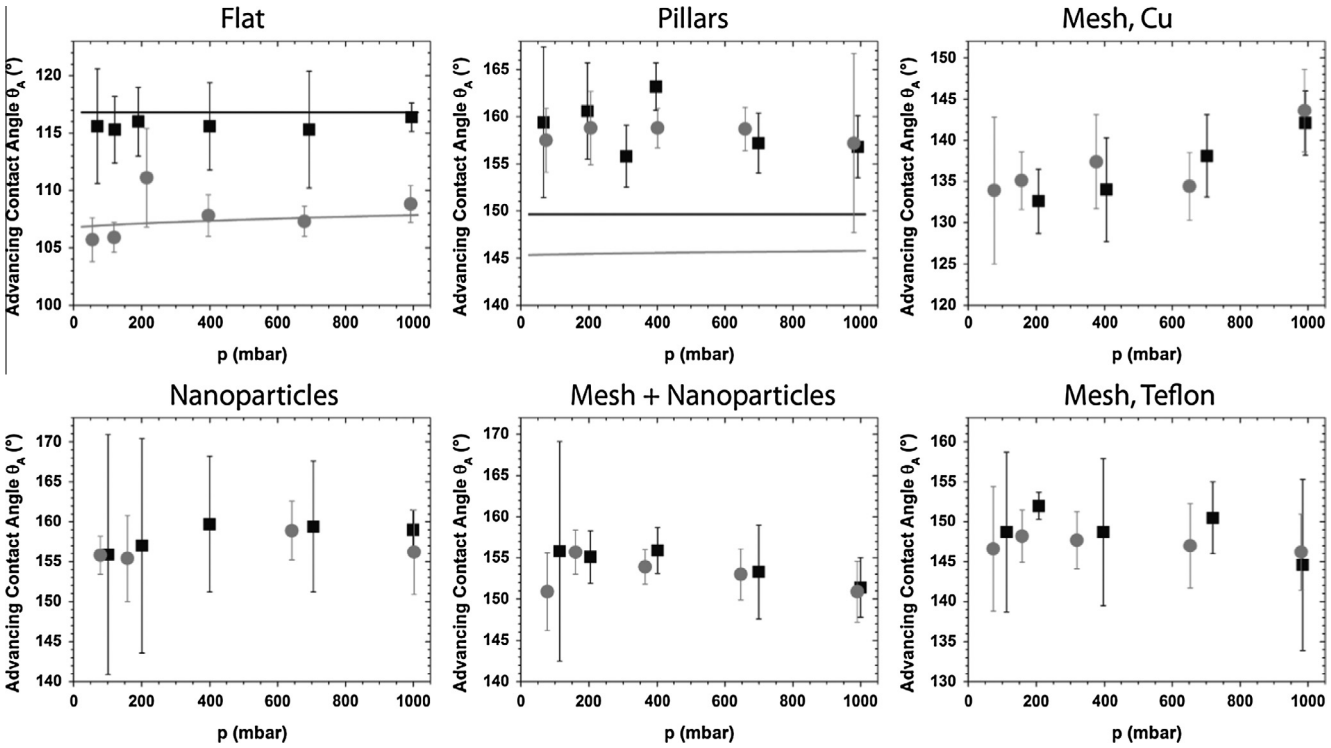

Fig. 4. Advancing static contact angles of water droplets in air (black) and water vapor (gray) as a function of pressure for the different sample types. In the water vapor environment, the temperature is adjusted to achieve saturation. For the flat, Teflon coated Si wafer, the model predictions for air and water vapor with an adsorption fitting parameter in vapor of $|\pi/\gamma_{lg}| = 0.16$ are included. For the 10×20 µm^2 (pillar size × pitch) square Teflon coated Si pillars, the model data for the Cassie–Baxter states is shown. The nanoparticles are a 1:1 ZnO:PDMS mixture in weight, and the mesh is a copper 200 mesh. Except for one bare copper mesh all samples are Teflon-coated. The error bars represent the 95% confidence interval as determined with a *t*-distribution.

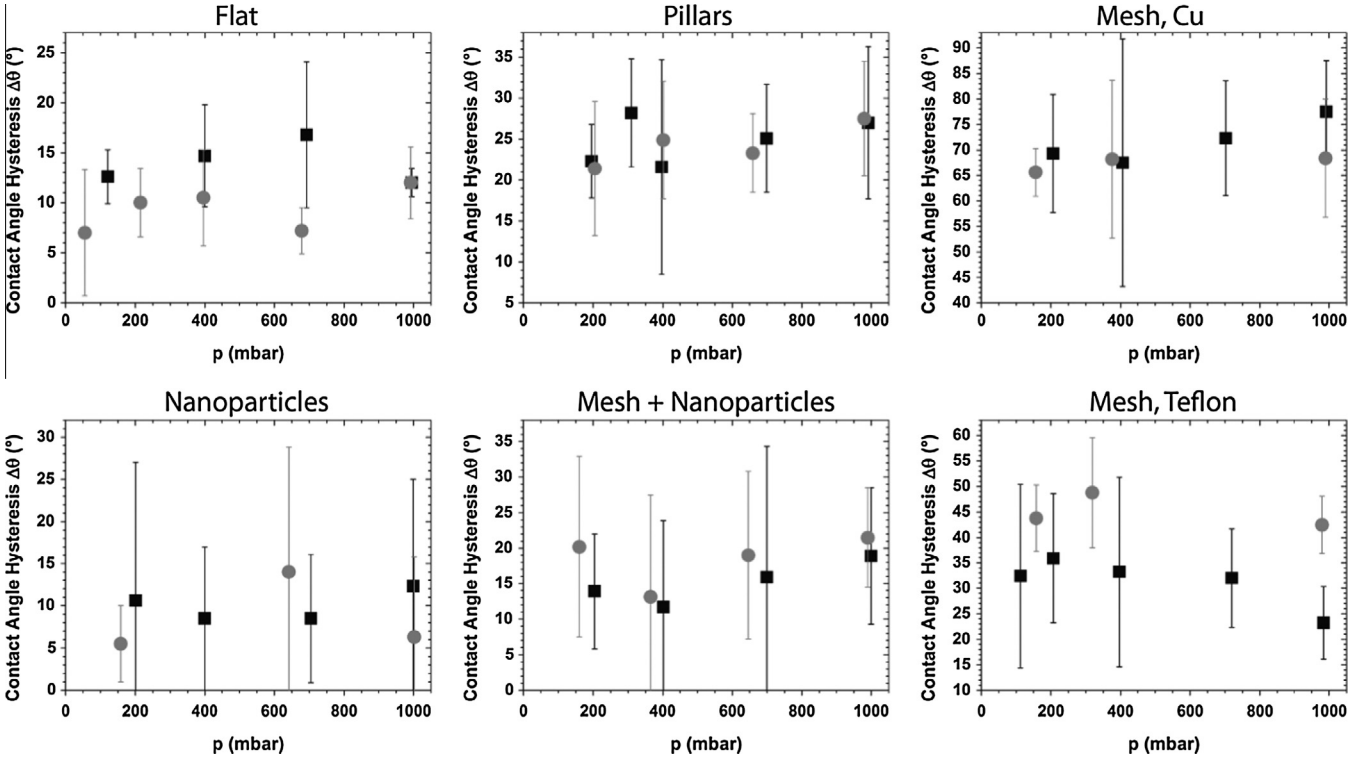

Fig. 5. Contact angle hysteresis of static water droplets in air (black) and water vapor (gray) as a function of pressure for the different sample types. In the water vapor environment, the temperature is adjusted to achieve saturation. The error bars represent the 95% confidence interval as determined with a *t*-distribution.

Table 1
Summary of static and dynamic advancing contact angles Θ_A and hysteresis $\Delta\Theta$ in degrees in air and water vapor environments. The values are averaged over all pressures and temperatures. The 95% confidence interval (±) of a measurement series is given in parentheses in degrees. Droplets on the meshes, both bare and Teflon-coated, are sticky and therefore have no dynamic contact angles.

Sample	Static, in air ($\theta_A - \Delta\theta$)	Static, in water vapor ($\theta_A - \Delta\theta$)	Dynamic, in air ($\theta_A - \Delta\theta$)	Dynamic, in water vapor ($\theta_A - \Delta\theta$)
Flat	116 (0.9) – 13 (1.1)	107 (0.7) – 10 (1.3)	120 (0.6) – 12 (0.6)	112 (1.3) – 17 (1.5)
Pillars	159 (1.2) – 25 (2.3)	158 (1.1) – 24 (2.5)	161 (0.6) – 27 (1.0)	162 (0.7) – 29 (1.3)
Nanoparticles	158 (1.9) – 10 (2.9)	157 (1.7) – 9 (3.2)	160 (1.1) – 5 (1.2)	154 (1.1) – 7 (1.3)
Mesh + Nanoparticles	154 (1.3) – 14 (3.3)	153 (1.1) – 19 (3.7)	157 (1.5) – 11 (2.0)	152 (2.2) – 10 (2.6)
Mesh, Teflon	149 (1.9) – 31 (3.2)	147 (1.5) – 45 (3.3)	–	–
Mesh, Cu	137 (1.9) – 72 (4.0)	137 (2.0) – 67 (3.1)	–	–

3.2. Modelling the static contact angles

Fig. 4 shows the prediction of the static CAs of water droplets on a flat Teflon surface. The predicted values match well with the measured advancing CAs in air. Since Teflon is highly non-polar, the interfacial energy between the solid and the liquid, γ_{sl}, in Young's equation (Eq. (1)) can be approximated with Fowkes' relationship for the additivity of intermolecular forces [35]

$$\gamma_{sl} = \gamma_s + \gamma_l - 2\sqrt{\gamma_s^d \gamma_l^d} \tag{4}$$

where γ_s and γ_l are the surface tensions of the solid and liquid, respectively, in vacuum (or air) and the superscript d denotes the dispersive components of the surface tension. At room temperature, the surface tension of water is $\gamma_l = \gamma_{lg} = 72.4$ mN/m, and Teflon has a surface energy of $\gamma_s = \gamma_{sg} = 20$ mN/m. The dispersive components for water and Teflon are $\gamma_l^d = 21.8$ mN/m and $\gamma_s^d = 18.6$ mN/m, respectively [36]. The interfacial energy between Teflon and the water droplet is then $\gamma_{sl} = 52.1$ mN/m at room temperature. The changes of surface tension with respect to temperature can be approximated with a linear fit. The temperature coefficient for water is $\Delta\gamma_l = -0.17$ mN/m K and for Teflon $\Delta\gamma_s = -0.06$ mN/m K. The changes in surface tension with pressure are negligible [37].

For droplets in the pure water vapor environment, a spreading pressure π must be introduced that accounts for vapor adsorption to the solid surface [38]. The net solid–gas surface tension becomes

$$\gamma'_{sg} = \gamma_s - \pi \tag{5}$$

Normalization with the temperature dependent surface tension of water, γ_{lg}, and combination with Young's equation yields

$$\cos(\theta) = \frac{\gamma_s - (-\pi/\gamma_{lg})\gamma_{lg} - \gamma_{sl}}{\gamma_{lg}} \tag{6}$$

Here, $(-\pi/\gamma_{lg})$ serves as a fitting parameter to match the experimental results. The negative sign indicates that water vapor adsorption increases the net surface energy of the solid. On the flat surface, $|\pi/\gamma_{lg}| = 0.16 = 16\%$, as shown by the gray solid line in the upper left graph of Fig. 4. This number can be interpreted as the area percentage of water vapor adsorption onto Teflon. Even though Teflon is hydrophobic, it has some hydrophilic sites that readily adsorb water molecules [39,40]. Since Teflon has a very low surface energy, many researchers have doubted, based on

theoretical considerations, that water could adsorb to the surface of the polymer and increase its net surface energy [38,39,41]. However, it has been shown previously that water, in fact, does actively adsorb to Teflon/PTFE surfaces [39,40,42,43]. The present findings are slightly higher than the values reported in literature, which range from $|\pi/\gamma_{lg}| = 8–12\%$ at room temperature [39,40,42,43].

Combining the model for the flat surface (Eqs. 1, 4 and 6) with the Cassie–Baxter equation (Eq. (3)) gives a prediction of CAs on pillars, as represented by the solid lines in the upper right graph in Fig. 4. The Cassie model under-predicts the experimental values for advancing CAs on pillars by 6% in air and by 8% in water vapor. A possible reason for the mismatch between model and data are fine ripples at the side walls of the pillars that formed during the Bosch etching process. These small waves act as re-entrant structures and increase the apparent CAs compared to those on smooth walls [44].

3.3. Dynamic contact angles

Figs. 6 and 7, and Table 1 present the dynamic advancing CAs and CAH for droplets on the flat sample, pillars and the two samples with nanoparticles. Droplets on the mesh-only samples were sticky and thus do not have dynamic CAs. In air, the advancing CAs are higher for moving droplets than for sessile ones. Except for on the pillars, the dynamic advancing CAs are lower in the water vapor environment than in air. Again, water vapor adsorption to the surface is the most probable explanation for the reduction in CA. At the same time, the dynamic receding CAs on the pillars decrease, which is consistent with previous experiments on flat or microgrooved surfaces where dynamic advancing CAs usually increased but dynamic receding CAs decreased or stayed constant with increasing droplet velocity [17,45–47]. On the flat surface and the nanoparticle samples, however, receding CAs increase in the dynamic regime. The reason for this increase is unknown. A possible explanation lies in the mode of the droplet movement. The study of movies of the displacing droplets at 1/6 of their original speed (see Supplementary Material) suggest that the droplets on the flat surface slide, but those on the micro-structured surfaces roll down the sample. We propose that – similar to a solid sliding along another solid – water droplets have two different friction coefficients. Sessile water droplets experience a static friction coefficient, while moving droplets are in the regime of the lower kinetic friction. Sticking of the contact line, i.e. static friction, results from the capillary force ($\pi\ a\ \gamma_{lv}$ ($\cos\Theta_R - \cos\Theta_A$); where a is the radius of the macroscopic contact area between droplet and solid) being greater than the weight of the droplet ($V\ \rho\ g \sin\alpha$) [48]. For moving droplets on a surface with low CAH, the term ($\cos\Theta_R - \cos\Theta_A$) is small and pinning of the contact line becomes less important.

Fig. 8 shows water droplets rolling down an inclined nanoparticle sample at two different velocities. At the lower rolling velocities in the left image the droplet shape is close to that of a sphere, with the dynamic advancing CA being greater than the receding CA. However, at a higher velocity, i.e. higher tilt angle, the droplet distorts and develops a hump at the upper rear flank of the droplet. Interestingly, the apparent dynamic receding CA appears to be higher than the dynamic advancing CA. The seeming reversion of the advancing and receding CA suggests that inertia is dominant over friction.

Table 2 summarizes tilt angles and average droplet velocities. On all samples, tilt angles were higher in the water vapor environment than in air and decreased slightly with decreasing pressure in both environments. On the flat surface, the average velocity for the

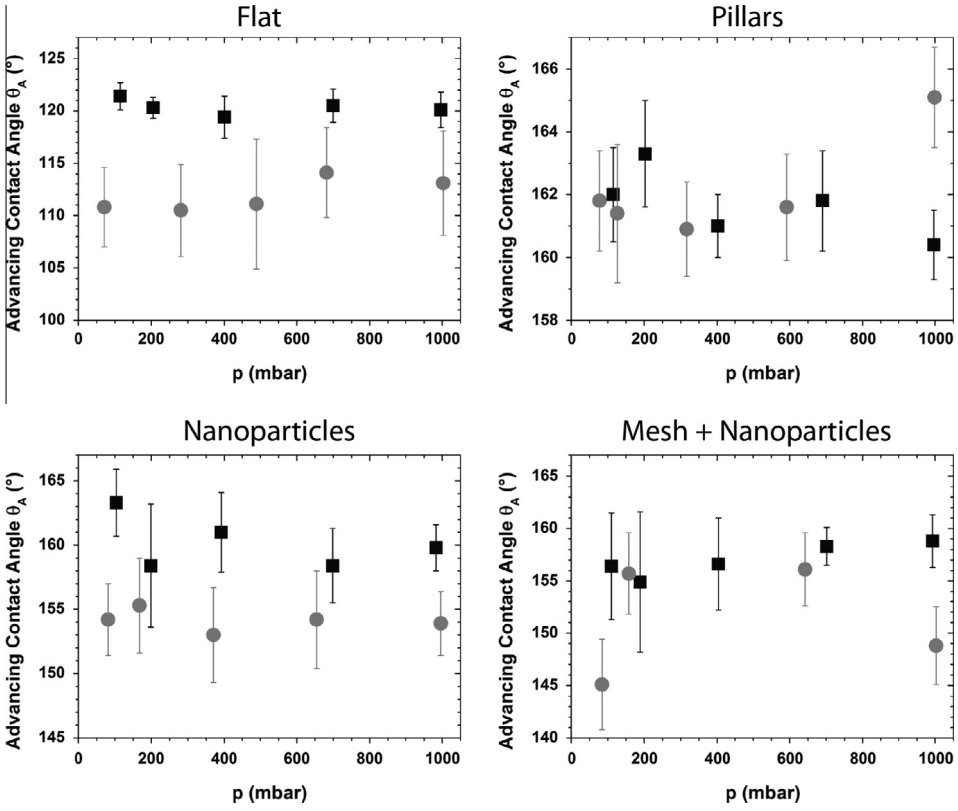

Fig. 6. Advancing dynamic contact angles of water droplets in air (black) and water vapor (gray) at saturation conditions as a function of pressure for the samples with a sliding angle $\alpha < 45°$. The inclination of the samples was 1–2° above the critical sliding angle. The error bars represent the 95% confidence interval as determined with a *t*-distribution.

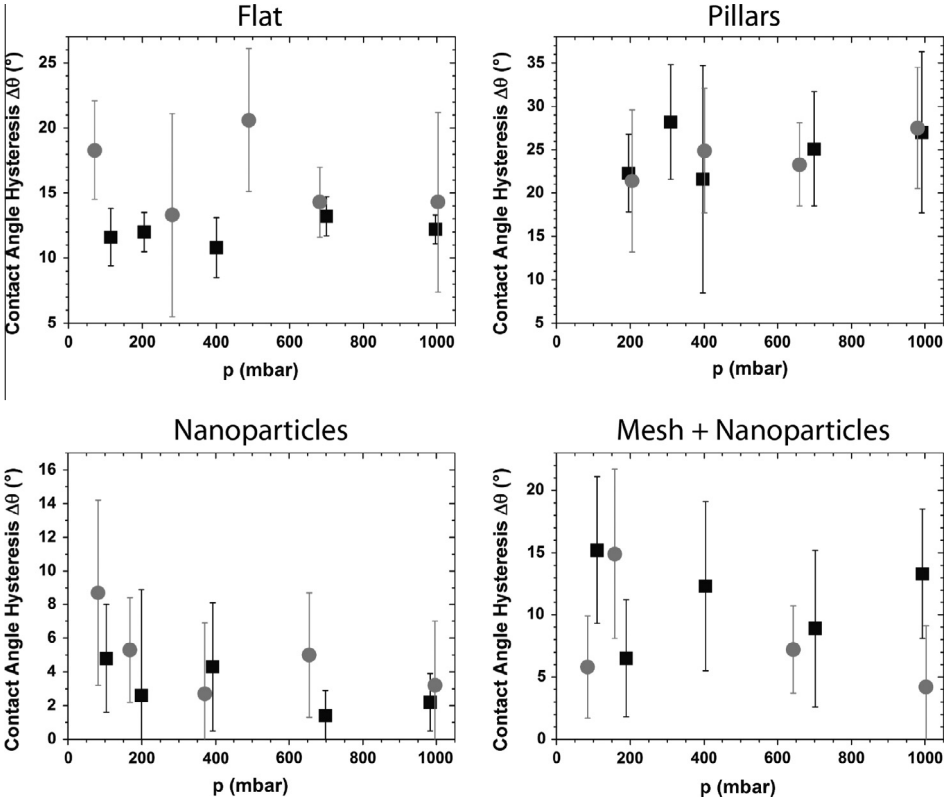

Fig. 7. Contact angle hysteresis of dynamic water droplets in air (black) and water vapor (gray) at saturation conditions as a function of pressure for the samples with a sliding angle $\alpha < 45°$. The inclination of the samples was 1–2° above the critical sliding angle. The error bars represent the 95% confidence interval as determined with a *t*-distribution.

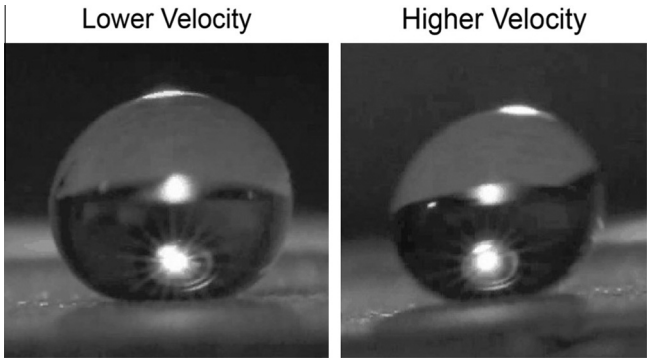

Fig. 8. Comparison of the shapes and contact angles of water droplets rolling down a 1:1 ZnO:PDMS nanoparticle sample at different velocities. At low velocities, the droplets are almost spherical with the advancing contact angle greater than the receding contact angle. At higher velocities the droplets distort and develop a hump at the rear flank. The dynamic receding contact angle appears greater than the advancing contact angle.

Table 2
Average tilt angles α and droplet velocities $\bar{u}$ for dynamic contact angle measurements with a droplet volume $V \approx 5$ µl.

Sample	Tilt angle α (°)	Average droplet velocity $\bar{u}$ (mm/s)
Flat	37.5 ± 2.5	3.5 ± 2
Pillars	18 ± 1	11 ± 3
Nanoparticles	4 ± 2	70 ± 6
Mesh + Nanoparticles	9 ± 2	148 ± 16

sliding droplet is 3.5 mm/s. Even though CAH is higher for the mesh + nanoparticle sample than for nanoparticles only, the former had the highest droplet velocities of about 148 mm/s. The reason for the faster droplets is the significantly higher tilt angle that was necessary for droplet movement.

4. Conclusion

We present measurements of static and dynamic contact angles in an air and a pure water vapor environment. For water droplets on flat or micro- and nanostructured hydrophobic surfaces, varying pressure, between 60 and 1000 mbar, and temperature, between 39 and 100 °C, have no significant effect on the measured contact angles. On a flat, Teflon-coated surface, static contact angles are lower in the water vapor environment than in air. We propose that vapor adsorption to the Teflon increases the effective surface energy of the solid. While some prior theoretical work concludes that water is not able to adsorb to the low-energy surface of Teflon, our findings match well with adsorption measurements on Teflon or PTFE surfaces reported in literature [39,40,42,43]. On micro- and nanostructured surfaces, static contact angles are similar in air and in water vapor.

In air, dynamic advancing contact angles are slightly higher than the respective static contact angles. In the water vapor environment, the dynamic advancing contact angles on a flat surface and on pillars are higher than in the static case, but lower than for sessile droplets on the samples with nanoparticles. Again, water vapor adsorption to the surface is likely to be the reason for the decrease in advancing contact angles. Interestingly, contact angle hysteresis decreases on the superhydrophobic nanoparticle samples when transitioning from static to dynamic contact angles. Fig. 9 summarizes the different surfaces with static and dynamic droplets at low droplet velocities. Future work should extend the range of droplet velocities and nanoparticle sizes to gain a better

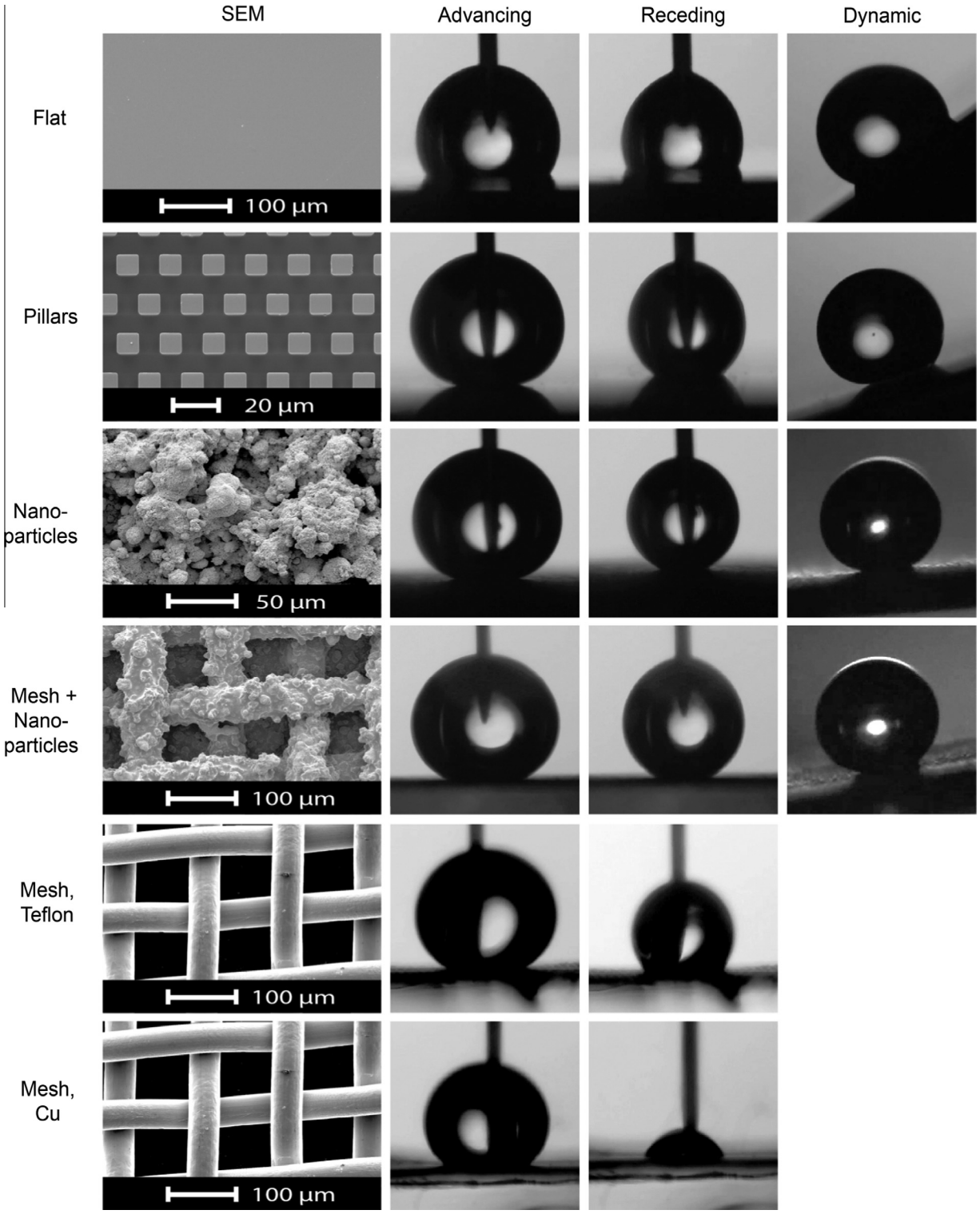

Fig. 9. Summary of the sample geometries (left) and advancing, static (center left), receding, static (center right) and dynamic (right) water droplets with $V \approx 5$ µl on all samples. Note that the droplets on the meshes were sticky, i.e. non-mobile, and thus do not have dynamic contact angles.

understanding of the influence and mechanism of water vapor adsorption in cavities on the surface.

Acknowledgments

We thank the staff from the Microscopy Suite at the Beckman Institute for their assistance. This work has been supported by the Office of Naval Research N00014-12-1-0014 and in part by the NSF (DMR-1206355).

Appendix A. Supplementary material

Supplementary data associated with this article can be found, in the online version, at http://dx.doi.org/10.1016/j.jcis.2015.04.060.

References

[1] C.-H. Chen, Q. Cai, C. Tsai, C.-L. Chen, G. Xiong, Y. Yu, Z. Ren, Appl. Phys. Lett. 90 (17) (April 2007) 173108.
[2] X. Chen, J. Wu, R. Ma, M. Hua, N. Koratkar, S. Yao, Z. Wang, Adv. Funct. Mater. 21 (24) (December 2011) 4617–4623.
[3] K. Rykaczewski, J.H.J. Scott, S. Rajauria, J. Chinn, A.M. Chinn, W. Jones, Soft Matter 7 (19) (September 2011) 8749–8752.
[4] R. Enright, N. Miljkovic, A. Al-Obeidi, C.V. Thompson, E.N. Wang, Langmuir 28 (40) (October 2012) 14424–14432.
[5] N. Miljkovic, R. Enright, Y. Nam, K. Lopez, N. Dou, J. Sack, E.N. Wang, Nano Lett. 13 (1) (2012) 179–187.
[6] R. Enright, N. Miljkovic, J.L. Alvarado, K. Kim, J.W. Rose, Nanoscale Microscale Thermophys. Eng. 18 (3) (July 2014) 223–250.
[7] J. Feng, Y. Pang, Z. Qin, R. Ma, S. Yao, ACS Appl. Mater. Interfaces 4 (12) (December 2012) 6618–6625.
[8] E. Schmidt, W. Schurig, W. Sellschopp, Tech. Mech. Thermodyn. 1 (2) (February 1930) 53–63.
[9] D. Attinger, C. Frankiewicz, A.R. Betz, T.M. Schutzius, R. Ganguly, A. Das, C.-J. Kim, C.M. Megaridis, MRS Energy Sustainab. 1 (2014). E4.
[10] D. Öner, T.J. McCarthy, Langmuir 16 (20) (October 2000) 7777–7782.
[11] B. Bhushan, Y.C. Jung, K. Koch, Philos. Trans. Roy. Soc. Math. Phys. Eng. Sci. 367 (1894) (May 2009) 1631–1672.
[12] L. Zhu, Y. Xiu, J. Xu, P.A. Tamirisa, D.W. Hess, C.-P. Wong, Langmuir 21 (24) (November 2005) 11208–11212.
[13] L. Gao, T.J. McCarthy, Langmuir 23 (7) (March 2007) 3762–3765.
[14] V. Kondrashov, J. Rühe, Langmuir 30 (15) (April 2014) 4342–4350.
[15] J. Yong, Q. Yang, F. Chen, D. Zhang, H. Bian, Y. Ou, J. Si, G. Du, X. Hou, Appl. Phys. A 111 (1) (April 2013) 243–249.
[16] W.-J. Jeong, M.Y. Ha, H.S. Yoon, M. Ambrosia, Langmuir 28 (12) (2012) 5360–5371.
[17] X. Wang, M.A. Rahman, A.M. Jacobi, R.S. Hrnjak, Heat Transf. Eng. 34 (13) (2013) 1088–1098.
[18] T. Darmanin, F. Guittard, RSC Adv. 4 (September 2014) 50401–50405.
[19] T. Young, Philos. Trans. Roy. Soc. Lond. 95 (1805) 65–87.
[20] L. Barbieri, E. Wagner, P. Hoffmann, Langmuir 23 (4) (February 2007) 1723–1734.
[21] L. Gao, T.J. McCarthy, Langmuir 22 (14) (July 2006) 5998–6000.
[22] L. Gao, T.J. McCarthy, Langmuir 22 (14) (July 2006) 6234–6237.
[23] L. Gao, T.J. McCarthy, Langmuir 25 (24) (December 2009) 14105–14115.
[24] S.S. Chhatre, W. Choi, A. Tuteja, K.-C. (Kenneth) Park, J.M. Mabry, G.H. McKinley, R.E. Cohen, Langmuir 26 (6) (March 2010) 4027–4035.
[25] R.N. Wenzel, J. Phys. Colloid Chem. 53 (9) (September 1949) 1466–1467.
[26] A.B.D. Cassie, S. Baxter, Trans. Faraday Soc. 40 (1944) 546–551.
[27] A. Tuteja, W. Choi, G.H. McKinley, R.E. Cohen, M.F. Rubner, MRS Bull. 33 (08) (2008) 752–758.
[28] A.F. Stalder, G. Kulik, D. Sage, L. Barbieri, P. Hoffmann, Colloids Surf. Physicochem. Eng. Asp. 286 (1–3) (2006) 92–103.
[29] J.-H. Song, M. Sakai, N. Yoshida, S. Suzuki, Y. Kameshima, A. Nakajima, Surf. Sci. 600 (13) (July 2006) 2711–2717.
[30] M. Sakai, J.-H. Song, N. Yoshida, S. Suzuki, Y. Kameshima, A. Nakajima, Surf. Sci. 600 (16) (August 2006) L204–L208.
[31] S. Lee, J.-S. Park, T.R. Lee, Langmuir 24 (9) (May 2008) 4817–4826.
[32] T. An, S.J. Cho, W. Choi, J.H. Kim, S.T. Lim, G. Lim, Soft Matter 7 (21) (October 2011) 9867–9870.
[33] A.T. Paxson, K.K. Varanasi, Nat. Commun. 4 (February 2013) 1492.
[34] A. Steele, I. Bayer, S. Moran, A. Cannon, W.P. King, E. Loth, Thin Solid Films 518 (19) (2010) 5426–5431.
[35] F.M. Fowkes, J. Phys. Chem. 67 (12) (1963) 2538–2541.
[36] D.H. Kaelble, J. Adhes. 2 (2) (1970) 66–81.
[37] R. Massoudi, A.D. King, J. Phys. Chem. 78 (22) (October 1974) 2262–2266.
[38] V.P. Carey, Liquid–Vapor Phase-Change Phenomena: An Introduction to the Thermophysics of vaporization and condensation in Heat Transfer Equipment: An Introduction to the Thermophysics of Vaporization & Condensation in Heat Transfer Equipment, Taylor & Francis, 1992.
[39] F.M. Fowkes, D.C. McCarthy, M.A. Mostafa, J. Colloid Interface Sci. 78 (1) (November 1980) 200–206.
[40] J.H. Chessick, F.H. Healey, A.C. Zettlemoyer, J. Phys. Chem. 60 (10) (October 1956) 1345–1347.
[41] R.J. Good, L.A. Girifalco, J. Phys. Chem. 64 (5) (May 1960) 561–565.
[42] P. Hu, A.W. Adamson, J. Colloid Interface Sci. 59 (3) (May 1977) 605–614.
[43] M.E. Schrader, Langmuir 12 (15) (1996) 3728–3732.
[44] H. Zhao, K.-Y. Law, V. Sambhy, Langmuir 27 (10) (May 2011) 5927–5935.
[45] R.E. Johnson Jr., R.H. Dettre, D.A. Brandreth, J. Colloid Interface Sci. 62 (2) (November 1977) 205–212.
[46] E.B. Dussan, Annu. Rev. Fluid Mech. 11 (1) (1979) 371–400.
[47] B. Krasovitski, A. Marmur, Langmuir 21 (9) (April 2005) 3881–3885.
[48] D. Richard, D. Quéré, EPL Europhys. Lett. 48 (3) (November 1999) 286.